Monthly Notices of the ROYAL ASTRONOMICAL SOCIETY

MNRAS **498,** 1308–1318 (2020) doi:10.1093/mnras/staa2379
Advance Access publication 2020 August 26

Temporal evolution of the permanent shadowed regions at Mercury poles: applications for spectral detection of ices by SIMBIOSYS-VIHI on BepiColombo mission

Gianrico Filacchione [1]★ Alessandro Frigeri,[1] Andrea Raponi,[1] Mauro Ciarniello,[1] Fabrizio Capaccioni,[1] Maria Cristina De Sanctis,[1] Cristian Carli,[1] Valentina Galluzzi,[1] Gabriele Cremonese,[2] Alice Lucchetti,[2] Cristina Re[2] and Matteo Massironi[3]

[1]*INAF-IAPS, via del Fosso del Cavaliere, 100, I-00133 Rome, Italy*
[2]*INAF-Padua Astronomical Observatory, Vicolo dell'Osservatorio, 5, I-35122 Padua, Italy*
[3]*Department of Geosciences, Padua University, via G. Gradenigo, 6, I-35131 Padua, Italy*

Accepted 2020 August 6. Received 2020 August 5; in original form 2020 June 23

ABSTRACT

Radar observations from the Earth and multi-instrument measurements by MESSENGER mission have indicated the presence of large quantities of ices within the permanent shadowed regions (PSRs) located at Mercury poles. The detection and mapping of the distribution of volatile species on PSRs are among the primary scientific goals of the Spectrometer and IMagers for MPO Bepicolombo Integrated Observatory SYStem (SIMBIO-SYS) suite aboard ESA's BepiColombo mission. We report about a three-steps preparatory study mainly focusing on SIMBIO-SYS/Visible and near Infrared Hyperspectral Imager (VIHI) 0.4–2.0 μm imaging spectrometer aiming (1) to render the solar illumination temporal evolution occurring on polar regions and in particular on Prokofiev and Kandinsky craters by studying the effects of shadows and penumbras caused by the finite apparent solar disc; (2) to simulate the spectral reflectance of various mixtures of average Mercury terrain and water ice in the spectral range of the VIHI imaging spectrometer channel in direct illumination, penumbra and shadowed illumination conditions; and (3) to verify the resulting VIHI signal-to-noise ratio during the different phases of the BepiColombo mission.

Key words: astronomical instrumentation, methods and techniques – planets and satellites: individual: Mercury surface.

1 INTRODUCTION

Permanent Shadowed Regions (PSRs) are sectors associated with craters, depressions, and fault scarps located on the surfaces of airless bodies that are never directly reached by solar flux, as a consequence of local rough topography, high latitude, and small rotation axis obliquity, equal to about 2 arcmin for Mercury (Siegler, Bills & Paige 2013). The existence of PSRs was first postulated by Watson, Murray & Brown (1961a,b) at the poles of the Earth's Moon and Mercury and later confirmed by radar observations from the Earth and by remotely sensed data returned by interplanetary probes that have observed water ice within many PSRs. This is possible because cryogenic temperatures can be stably maintained in these cold traps: for an atmosphereless body like Mercury, despite the orbit vicinity to the Sun, surface temperature in some PSRs is permanently below 120 K (Paige et al. 2013) allowing to preserve frozen volatiles across geological time-scales. The total surface area in permanent shadowed condition a the South Pole between latitude -80° and -90° is estimated in about 25.000 km^2 (Deutsch et al. 2016; Chabot, Shread & Harmon 2018), about two times larger than on the same geographic area on the North Pole. The large extension of these areas is a consequence of the rough surface's morphology, with craters' depth up to about 3 km and very high solar incidence angles (Chabot et al. 2018).

Both Radar observations from the Earth and multi-instrument measurements by MESSENGER mission have demonstrated the presence of large quantities of ices within many PSR located at Mercury poles. Starting from 90s several, different techniques have confirmed that PSR are enriched in water ice. A first method used was the study of the polarization ratio of scattered radar waves that are responsive to the nature of the target. This technique has been employed by Slade, Butler & Muhleman (1992) and Harmon et al. (1994) who found that radar waves reflected from Mercury polar craters show an intense circular polarization that is a specific response of very rough terrains or water ice-rich surfaces. However, Paige, Wood & Vasavada (1992) pointed out that both local thermal properties of the surface and morphology of the craters were in favour of the water ice enrichment as a possible cause of the observed circular polarization. Further observations at different radar wavelengths (*X* band from Goldstone and *S* band from Arecibo radiotelescopes) on the same craters have shown minimal dependence from wavelength thus supporting the hypothesis that the water ice deposits are covered by a roughly 10-cm-thick surface layer (Harmon, Slade & Rice 2011). Further evidences of the nature and distribution of hermean polar ices were obtained by some instruments aboard the NASA MESSENGER mission (Solomon et al. 2007). The emission of epithermal neutrons from north pole

★ E-mail: gianrico.filacchione@inaf.it

appears compatible with a local enrichment of hydrogen in water ice, while fast neutron flux allows to localize lag deposits, generally at lower latitudes, where ice is buried below a less hydrogen-rich surface layer (Lawrence et al. 2013). This layer, characterized by low albedo on visible images, could be the residual of volatiles sublimation and probably enriched in carbon bearing material (Paige et al. 2013). Conversely, ice-rich PSRs are characterized on images by sharp boundaries and distinctive reflectances possibly indicating a recent formation (Chabot et al. 2014, 2016). MESSENGER Laser Altimeter (MLA; Cavanaugh et al. 2007) operating with an active laser emitting at wavelength of 1064 nm was able to detect ice deposits within PSR independently from their solar illumination and to map their topographical distribution (Neumann et al. 2013). In agreement with neutron data, on MLA observations the exposed deposits are brighter than the average anhydrous terrain, while buried deposits appear darker (Deutsch, Neumann & Head 2017). Ice deposits are distributed at every spatial scale encompassing large (≈100 km) impact craters (Chabot et al. 2014, 2018; Deutsch et al. 2017), smaller (1–10 s km) craters and rough terrain units (Deutsch et al. 2017), to metre-sized cold traps (Rubanenko et al. 2018). Apart water ice, other compounds have been suggested taking into account the visible reflectance and the cryogenic environments associated with PSRs, as C-rich materials, Ar, SO_2, S, or organic compounds (Paige et al. 2013). Unfortunately, no compositional measurements through spectroscopy were possible with the MESSENGER payload.

Exogenic, endogenic, and solar implantation processes have been proposed to explain the presence of Mercury's icy polar deposits. In the exogenic scenario, ices were carried from the outer to inner Solar system by comets, asteroids, and micrometeorites impacting Mercury's surface (Ernst, Chabot & Barnouin 2018). In the endogenic scenario, polar ices are formed by condensation of volatiles in cold traps during intense volcanic outgassing events (Head et al. 2011) and during the possible development of a global magma ocean (Vander Kaaden & McCubbin 2015). Finally, water could be thermally synthesized from OH bound to mineral species through the implantation of solar-wind protons (Jones, Sarantos & Orlando 2020).

In general, the study of the distribution, composition, and volume of the ices within PSRs is of paramount importance to understand their origin, transport, accumulation, and evolution. Although MESSENGER mission has allowed to greatly improve our knowledge of the distribution of the PSRs, it lacks of high spatial resolution and global coverage data to better map and constrain the overall composition and mass of the ices. In this respect, the detection, mapping, and retrieval of the composition of volatile species in PSRs are among the primary scientific goals of the Spectrometer and IMagers for MPO Bepicolombo Integrated Observatory SYStem (SIMBIO-SYS) suite (Cremonese et al. 2020) aboard ESA's BepiColombo mission (Benkhoff 2020). BepiColombo/Mercury planet orbiter (MPO) spacecraft is designed to operate from an elliptical inertial polar orbit around Mercury with an apocenter at 1500 km and a pericenter at 480 km altitude at the beginning of the mission decreasing to 400 km at the end. The nominal period of the orbit is about 2.3 h. A schematics of the BepiColombo orbit characteristics is shown in Fig. 1

SIMBIO-SYS employs three optical channels in parallel, each of them providing different data of the surface: (1) the high resolution imaging channel (Zusi et al. 2019) will return high-resolution visible-colour images (through 550, 750, 880 nm, and panchromatic filters) of about 20 per cent of Mercury's surface area at pixel scale ≤12 m px^{-1}, (2) the STereoscopic imaging Channel (STC; Da Deppo et al. 2010) will return the global digital terrain model (DTM) using

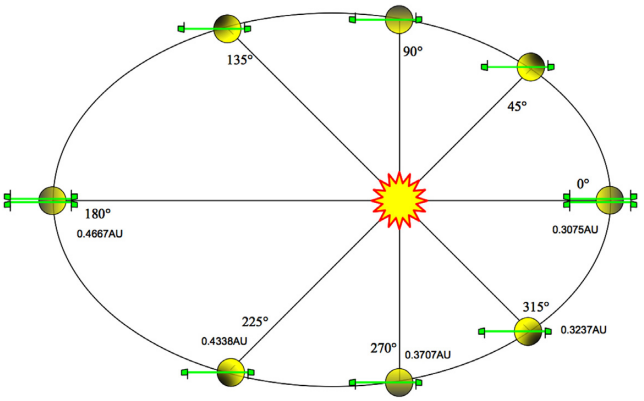

Figure 1. Schematics of Mercury and BepiColombo spacecraft orbits (the green lines) seen from the Sun's North Pole. At TA = 0°, Mercury is at perihelion and the spacecraft is at apoherm on the day side. At TA = 180°, Mercury is at aphelion and the spacecraft is at periherm on the day side.

the panchromatic filters with a pixel scale ≤120 m $pixel^{-1}$ and colour images (420, 550, 750, 920 nm) of selected regions, and (3) the Visible and near Infrared Hyperspectral Imager (VIHI, Capaccioni et al. 2010) will observe the entire Mercury surface in the 0.4–2.0 μm spectral range with a spectral sampling of 6.25 nm $band^{-1}$ and a pixel scale ≤500 m $pixel^{-1}$ with selected regions of interest observed at 120 m $pixel^{-1}$.

Taking advantage of the spectral range, sampling, and high sensitivity of the VIHI instrument we will investigate in this work the capability to identify and map ices in the hermean PSR by means of hyperspectral images. In doing this, we have considered the orbital characteristics of BepiColombo mission, the VIHI observation mode and the evolution of the illumination conditions occurring on polar regions during one solar day. To better constrain this scientific case, we report about a three-steps preparatory study aiming to

(i) simulate the solar illumination evolution during one hermean day on the north polar region and in particular on Prokofiev and Kandiscy craters where extended PSRs are located. In Section 2 is discussed the formation of shadows and penumbra in PSRs caused by the finite (not-point) dimension of the solar disc. In Section 3, we analyse the temporal illumination variations as a function of TA. The illumination is computed utilizing a ray-tracing code reproducing the Sun apparent position and angular diameter above the craters during a full hermean day. The craters' morphology is simulated from MLA digital elevation model (DEM) at 675 m resolution. Through this analysis, it is possible to determine at which TA occur the best transient conditions to observe areas neighbouring the PSR in a partially illuminated penumbra regime from BepiColombo's orbit.

(ii) derive syntethic I/F spectra of mixtures of the average hermean terrain and water ice in different abundances, mixing modes (areal, intimate), and grain sizes distribution at VIS–IR wavelengths within VIHI spectral range. These simulations are performed in two different illumination regimes: direct (Section 4) and indirect (Section 5), or scattered, sunlight. The penumbra case is modelled starting from the direct illumination case by applying an attenuation factor.

(iii) the simulated I/F spectra are used as inputs to perform VIHI signal-to-noise simulations with the scope to evaluate the VIHI capability to detect water ice in direct, penumbra, and indirect illumination conditions during the different observation phases of the BepiColombo mission (Section 6).

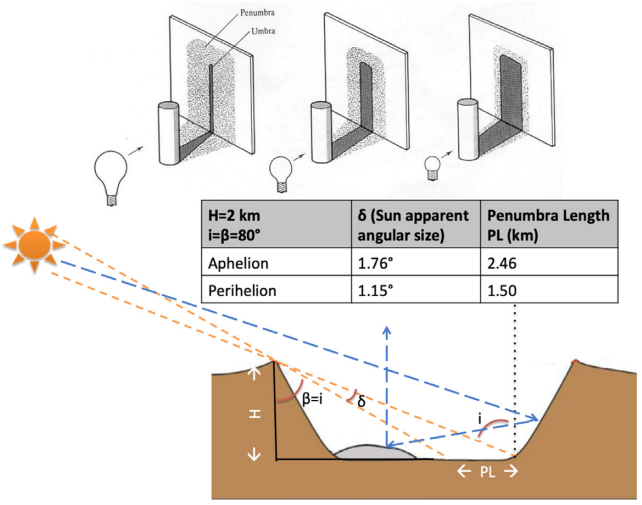

Figure 2. Top panel: umbra and penumbra cast by an extended source at finite distance. Centre table: penumbra length values for a crater's rim of height H = 2 km placed at latitude 80° at perihelion and aphelion. Bottom panel: penumbra geometry case (the orange lines) and indirect illumination case of an ice deposit within PSR by the illuminated rim of the crater (the blue lines, see discussion in Section 5).

A discussion of the results and future prospects of this work is given in Section 7.

2 PENUMBRA IN PERMANENT SHADOWED REGIONS

Reflectance imaging spectroscopy is used to derive composition and physical properties of a planetary surface by analysing the fraction of reflected solar light. For this reason, to maximize the signal good illumination and observation geometries are normally preferred corresponding to low incidence (i) and emission (e) angles in order to minimize the phase angle. This general paradigm cannot be achieved on Mercury polar regions where the solar rays are grazing the surface and the incidence angle is proximal to 90°. Apart from the reduction of the solar flux with latitude (β) that is proportional to $\cos(\beta) = \cos(\mathrm{i})$ for a spherical shape, the illuminated scene is affected by a dominance of shadowed regions caused by the grazing illumination on rough terrains. Due to a combination of very high cratered terrains and vicinity to the Sun, on Mercury polar regions are present peculiar shadow conditions.

Shadow cast by an object illuminated by an extended source placed at finite distance is made of a central 'umbra' surrounded by a blurred 'penumbra' (see Fig. 2, top panel). In general, when computing shadows on Solar system objects this effect is negligible because the Sun's apparent diameter is small. But this approximation is not more valid for Mercury because from its heliocentric distance the solar disc has an apparent angular size ranging between 1.15° at aphelion to 1.76° at perihelion. This means that the illumination conditions are not those of a point source at infinite distance (illuminating the surface with parallel rays) but of an extended source at finite distance (diverging beams). As a consequence of this effect, the projected shadow line is not a sharp edge but rather a blurred transition area whose dimension depends on the Sun apparent size.

For an obstacle of height H illuminated by the Sun at incidence angle i (corresponding to latitude β), the length of the penumbra

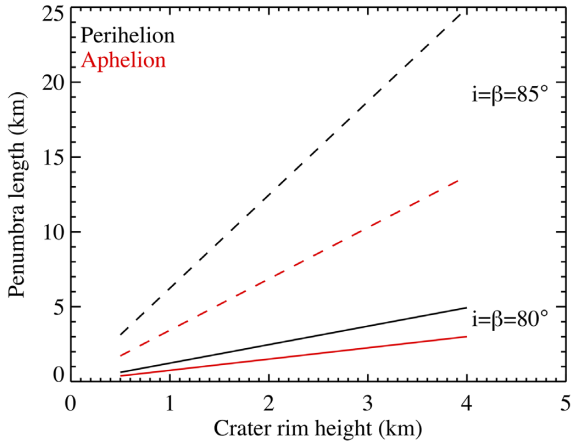

Figure 3. Penumbra length cast by the Sun at at perihelion (the black lines) and aphelion (the red lines) from a crater's rim of variable height between 0.5 and 4 km placed at latitude $\beta = 80°$ (the solid lines) and at $\beta = 85°$ (the dashed lines).

(PL) region is given by

$$PL = H[tg(\beta + \delta) - tg(\beta)], \quad (1)$$

where δ is the apparent diameter of the Sun (Fig. 2, bottom panel). The length of the penumbra on Mercury is not negligible reaching a length of 2.46 km at perihelion and 1.5 km at aphelion for the shadow casted by a crater's rim of 2 km height (as measured from the floor) placed at latitude ±80° (see Fig. 2, centre table). Moving towards poles shadows and penumbras length become longer and longer. As shown in Fig. 3, at a given latitude the length of the penumbra increases with the crater rim height and it is greater at perihelion than at aphelion. Due to the complex surface morphology and orbital characteristics, the illumination conditions change quite rapidly at Mercury's polar regions during one solar day. In this respect, the observation of PSR regions in penumbra conditions could offer a strategic advantage in the detection of surface ices through measurements of reflected light. Areas in penumbra in fact shall receive limited insolation flux for limited periods of time allowing to extend the visibility within PSRs and to search for ices.

3 ILLUMINATION CHANGES ON POLAR REGIONS

Solar illumination is rendered on the north pole DEM derived from MESSENGER publicly available data using ISIS procedures. In Fig. 4 is shown a polar projection of the illumination rendering occurring at TA = 200°. The method takes into account the finite dimension of the solar disc and Mercury orbital parameters during one hermean solar day and computes the resulting rendering assuming a uniform surface reflectivity. In the supplemental online material, we include the full animation rendered every 2° in TA from which is possible to follow the time evolution of the illumination conditions above the north polar regions. This simulation allows to trace the illumination evolution across specific PSRs, such as the ones located in Kandinsky (K) and Prokofiev (P) craters labelled in Fig. 4, which we have used as test cases. These two craters are very close to the North Pole and have very high rims (Kandinsky is located at 87.89°N 78.78°E, diameter 60 km, height ≈3 km; Prokofiev is at 85.77°N 62.92°E, diameter 112 km, height ≈3 km) to maintain large exposed water ice deposits on their floors.

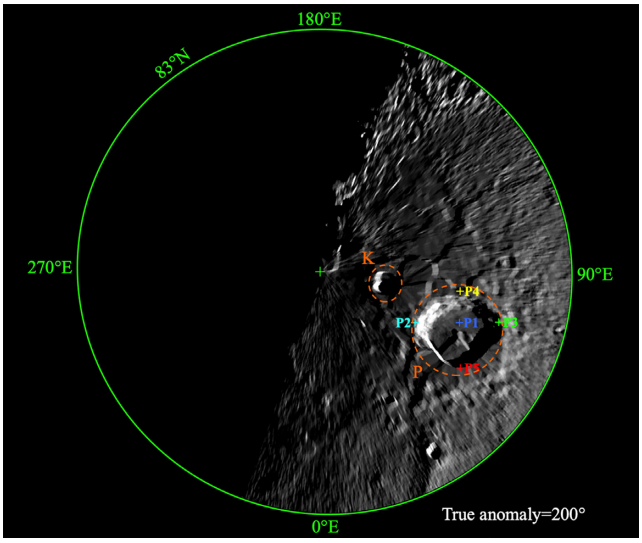

Figure 4. Illumination rendering on the north polar regions for TA = 200°. The full simulation covering an entire solar day is available as a supplemental online material. Locations P1–P5 are shown for Prokofiev (similar positions for Kandinsky are shown in Fig. 9) at larger scale.

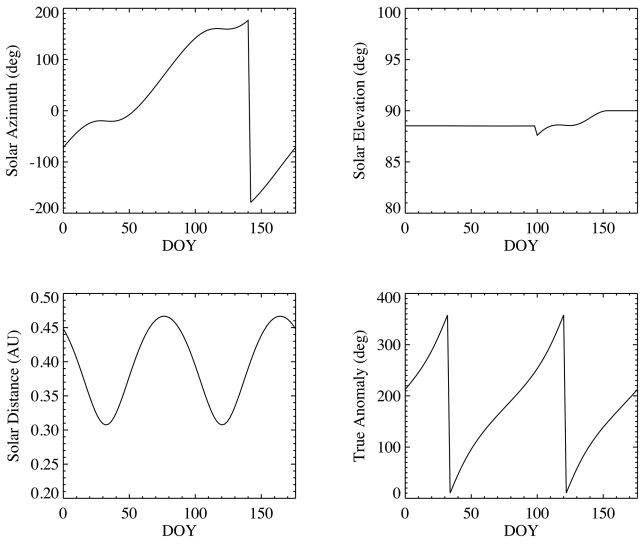

Figure 5. Average illumination conditions above Prokofiev and Kandinsky craters and Mercury's orbital parameters for one hermean solar day. The illumination rendering shown in the previous Fig. 4 at TA = 200° corresponds to DOY = 84.

The average illumination conditions occurring during one solar day on Kandinsky and Prokofiev craters and Mercury's orbital parameters are shown in Fig. 5). For each of the two craters, four areas corresponding to the crater' centre (position 1) and four locations on the rim (positions 2, 3, 4, 5) are analysed. The variation of the illumination conditions above them, traced by means of the cosine of the solar incidence angle, or cos (*i*), as a function of time is shown in Fig. 6 during one hermean solar day (corresponding to 176 Earth's days or DOY on which the temporal simulation is computed).

The simulation shows that K1 point is never reached by the Sun's rays during the solar day period, while the four locations on the rims are partially illuminated for limited periods of time (see Fig. 6, left-hand panel): the best illumination is registered on area K5 that has maximum cos(i) = 0.83 at DOY 53. This

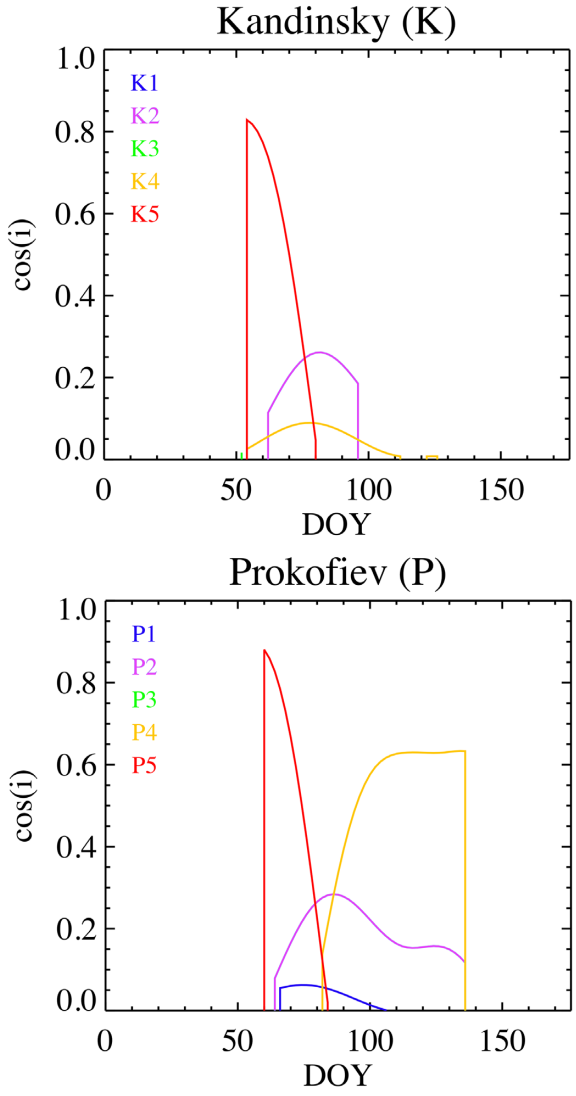

Figure 6. Illumination conditions above centre and rims of Kandinsky (top panel) and Prokofiev (bottom panel) craters locations #1–5 for one hermean solar day.

location undergoes to a progressive decrease of the incidence angle until becoming unilluminated on DOY = 80. The next best illuminated location is K2 that has a diurnal trend from DOY 62 to 96 with a maximum exposure at cos(i) = 0.26 on DOY = 81. Location K4 experiences the longest exposition to the Sun from DOY 53–136 with an interruption between DOYs 112 and 122. In this case, the maximum cos(i) = 0.09 is reached at DOY = 80. Finally, the worst illumination condition at cos(i) = 0.03 is observed by K3 at DOY 51. This point experiences also the shortest period of illumination, about 1 d.

Similar analysis performed on the much larger Prokofiev crater shows that location P3 on the south-east rim is never illuminated by the Sun during one solar day (see Fig. 6, right-hand panel). The crater centre P1 is scarcely illuminated (max cos(i) = 0.06) at DOY = 66 to return in shadow on DOY = 105. The highest illumination angle is reached on the rim at P5 where cos(i) = 0.88 at DOY = 60 to progressively moving into shadows at DOY = 83. Both P2 and P4 experience long exposures to the Sun, from DOY = 65–136 to –136, respectively. But while P4 maintains stable illumination

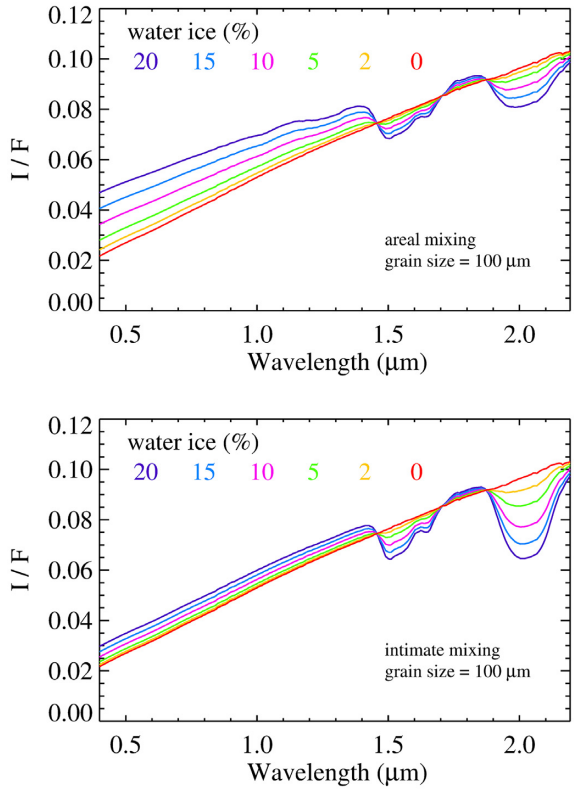

Figure 7. Simulated I/F spectra of AMT-water ice mixtures with relative abundances from 100:0 per cent to 80:20 per cent (areal mixture on top panel, intimate mixture on bottom) for 100 μm water ice grains diameter. Incidence angle is 80°, and emission angle is 0°.

(cos(i) = 0.6) across a wide plateau from DOY 100 to 136, P4 is characterized by two peaks at cos(i, DOY = 86)=0.28 and at cos(i, DOY = 125) = 0.17.

With this analysis, we have shown the importance of a temporal simulation to foresee the best illumination conditions occurring in the proximity of PSRs in order to properly plan SIMBIO-SYS observations from BepiColombo. Moreover, this analysis will be useful to compute thermal flux on the vicinity of PSR areas with the scope to constrain temporal stability of ices.

4 SPECTRAL SIMULATIONS ON DIRECT SUNLIGHT AREAS

Next, we derive synthetic spectra of water ice rich terrains on the polar regions of Mercury observed in direct sunlight geometries. This case is representative of transient illumination conditions occurring on areas normally placed within shadowed regions that become exposed for limited periods of time (see previous section). For this reason, a similar analysis needs the computation of the illumination conditions on a DEM of the area of interest. However, the detection of water ice in PSRs will be facilitated by the presence of diagnostic absorption features at 1.05, 1.25, 1.5, 1.65, 2.0 μm that are within the VIHI spectral range and resolution capabilities. Those features in general are well contrasted with respect to the average red slope characterizing Mercury terrain reflectance (see Fig. 7, the orange plot lines). Quantitative spectral modelling based on radiative transfer codes is applied to different mixtures of average Mercury terrain (AMT) and water ice, varying the abundances of the two endmembers, the water ice grain size, the mixing modality (areal and intimate), and the incidence angle. The modelling is based on Hapke's radiative transfer model (Hapke 1993):

$$r(i,e,g,\lambda) = \frac{w(\lambda)}{4\pi}\frac{\mu_0}{\mu_0+\mu}\left[B_{SH}\,p(g,\lambda) + H(w,\mu_0)H(w,\mu) - 1\right] \times B_{CB}(g,\lambda), \quad (2)$$

where r is the bidirectional reflectance, i, e, g are the incidence, emission, and phase angles, respectively; w is the single scattering albedo (SSA); $p(g, \lambda)$ is the single particle phase function, assumed isotropic ($p = 1$). This simplification probably introduces a little overestimate of the reflectance at high phase angles with respect to more rigorous phase functions derived from photometry (Domingue et al. 2019a,b) that needing to be tuned for different terrains units are excessive to be used for our purposes; $\mu_0 = \cos(i) = \cos(ZA)$ where the solar zenith angle (ZA) drives the illumination conditions for a given point at latitude (lat) on the Mercury surface for an orbital position defined by true anomaly TA (see Fig. 1):

$$ZA = a\cos(\cos(lat)\cdot abs(\cos(\pi - TA))) \quad (3)$$

as a case study we have fixed lat = ±80° in our simulations; $\mu = \cos(e)$, but since VIHI will observe in nadir mode $e = 0°$ and $\mu = 1$; $H(w, \mu_0, \mu)$ are the Ambartsumian–Chandrasekhar functions modelling the contribution of the multiple scattering; B_{SH} is the shadow-hiding opposition effect contribution; B_{CB} is the coherent back-scattering opposition effect contribution. With the exception of observations taken in opposition effect regime, e.g. when BepiColombo's is orbiting at Apoherm and Periherm (where $i = e = g = 0°$ at the equator), for the remaining cases the shadow hiding effect is negligible resulting in the simplification of terms $B_{SH} = 1$ and $B_{CB} = 1$.

The value of $w(\lambda)$ is modelled as the mixing of two components: (1) AMT, given by an intimate mixture of 75 per cent labradorite and 25 per cent enstatite of 30 μm average grain size and 0.1 wt per cent submicroscopic metallic iron distributed in grain coating (Warell & Blewett 2004). This endmember is a proxy of the average Mercury surface reflectance and its spectral radiance factor I/F by Warell & Blewett (2004) is scaled in $w(\lambda)$ by inverting Hapke's equation 2; (2) water ice at different relative abundances and mixing modalities. Water ice $w(\lambda)$ is computed for a given grain size starting from optical constants measured by Warren (1984) and Mastrapa et al. (2008) by applying the Hapke (2005) theory. The bidirectional reflectance (r) computed from equation (2) at a specific illumination and viewing geometry is finally converted in radiance factor:

$$I/F(\lambda) = \pi \cdot r(\lambda) \quad (4)$$

to allow a direct comparison with observations. Different mixing modalities between AMT and water ice are explored in the simulations (Ciarniello et al. 2011): (1) in areal mixing the observed photon is scattered only by one of the two endmembers, a condition corresponding to the presence of separate patches of AMT and water ice within the pixel. With this mixing, the observed reflectance is an average of the two endmembers weighted for their respective relative areal extension; (2) in intimate mixing (e.g. 'salt and pepper') the observed photon is scattered by both endmembers since the particles are in strict contact among them. In this case, the $w(\lambda)$ is an average of AMT and water ice SSAs weighted by their abundance (more precisely the geometrical cross-section by number density of each endmember). As a result of this method, the trends of the simulated reflectance for intimate and areal mixtures made of AMT with water ice grains of 100 μm diameter in abundance running from 0 to 20 per cent are shown in Fig. 7. Synthetic reflectance spectra of a mixture of AMT and water ice at a fixed abundance of 95:5 per cent for grains varying between 1 and 1000 μm in diameter are shown

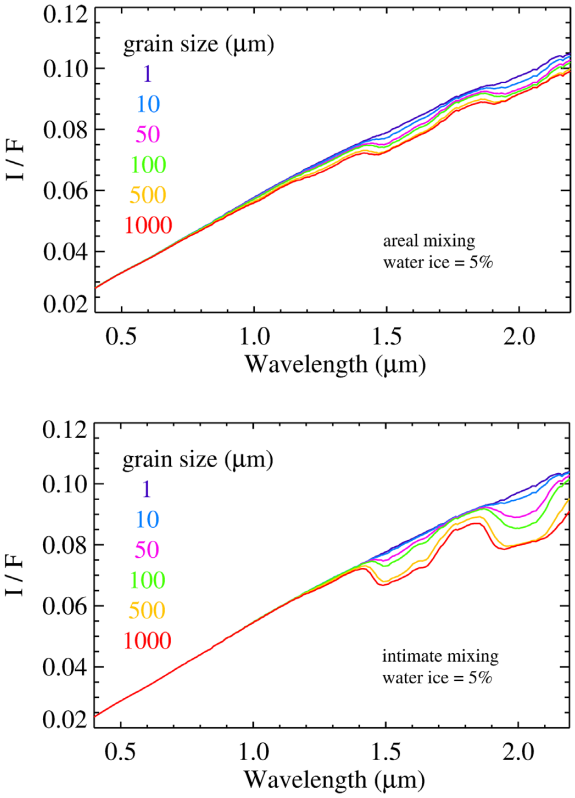

Figure 8. Simulated I/F spectra of AMT-water ice mixture with relative abundance 95:5 per cent (areal mix on the top panel, intimate mixing on bottom panel) for 1–1000 μm water ice grains diameters. Incidence angle is 80°, and emission angle is 0°.

in Fig. 8. All these I/Fs are computed for TA = 0° (Mercury at perihelion, BepiColombo at apoherm, see Fig. 1) for a point located at latitude ±80° observed with solar incidence angle $i = 80°$ and emission angle $e = 0°$ (nadir view). In general, we observe that the areal mixing cases show an increase of the I/F and a reduction (bluening) of the spectral slope across the 0.4–1.35 μm range with respect to the intimate mixing at parity of water ice enrichment (Fig. 7). The 1.5–1.65 μm band depth is similar between the two mixing modalities at parity of water ice abundance. Conversely, the 2 μm band is deeper in the intimate mixing case. The size of the water ice particles influences the I/F spectra in correspondence of the 1.5–1.65 and 2 μm bands: simulations in Fig. 8 show that large grains (1000 μm) cause stronger absorption with respect to small ones (1 μm). This effect is more evident on the intimate rather than on the areal mixing case.

Our spectral modelling demonstrate that VIHI has the capability to asses abundance, mixing modality, and grain size of water deposits in direct illumination conditions by measuring their I/F spectra. In the next section, we discuss how is it possible to extend this methodology to PSRs.

5 SPECTRAL SIMULATIONS ON SHADOWED AREAS

Photometric modelling in the proximity of shadows and through penumbra areas is a challenging task because apart the direct illumination gradients due to penumbras it is necessary to take into account for multiple scattered light coming from nearby illuminated areas. This effect is quite common on polar craters where a direct

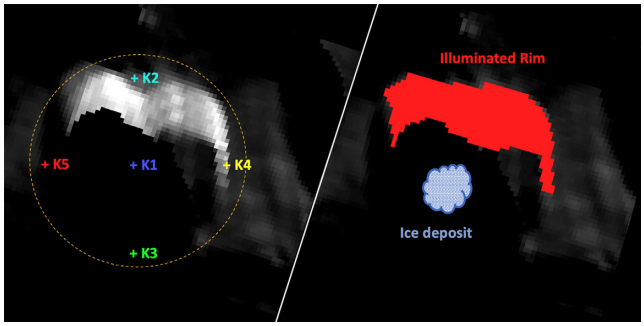

Figure 9. Simulated illumination conditions, or cos(i), occurring on Kandinsky crater at TA = 200° (left-hand panel). The area of the sun illuminated rim (in red, departing from point K2) and the location of the putative water ice deposit (the blue dots, corresponding to location K1) on the unilluminated crater floor are shown on the right-hand panel.

illuminated fraction of the rim could scatter light on the shadowed areas placed on the crater's floor and remaining rim. On these cases, it is possible to measure the reflectance of shadowed areas by replacing the solar spectral flux with the one reflected by the nearby illuminated areas. A similar approach has been successfully applied to detect ice variations on the unilluminated rim of Juling crater on Ceres by means of infrared spectroscopic measurements (Raponi et al. 2018). We use the same methodology to compute the I/F associated with a putative exposed water ice deposit located in the middle of Kandinsky crater for which we have evidences from MESSENGER MLA data (Neumann et al. 2013). As a test case we compute the resulting I/F for observations taken in VIHI observing geometries at TA = 200° for which the distribution of the *cos*(*i*) is shown in Fig. 9 (left-hand panel). We assume the ice deposit to be in the centre of the crater floor (point K1 marked by the blue dot area in Fig. 9, right-hand panel), illuminated by photons scattered by the crater rim (area in red on the same figure centred on point K2). The latter is directly illuminated by solar light, with an average incidence angle $<i> = 76°$ corresponding to $<\mu_0> = 0.267$. The angular extension of the illuminated rim as seen from the ice deposit is about 167° in azimuth and about $\alpha = 5.7°$ in elevation corresponding to a solid angle $\Omega \approx 0.1\ \pi$ sr. Higher orders of scattered light are assumed to be negligible.

To model the albedo of the light scattered from the crater rim regolith towards the shadowed ice-rich region, and the secondary scattered light from the latter towards the detector, we take into account the bi-hemispherical reflectance (r_s), which is a function of the optical constants of the two endmembers (Warell & Blewett 2004 for AMT; Warren 1984, Mastrapa et al. 2008 and Clark et al. 2012 for water ice) and the grain size, as discussed in Hapke (2005, 2012), assuming, for simplicity, that the reflectance of the surfaces can be described by the Lambert law. We model the crater rim regolith as devoid of ice, while the ice-rich region as pure water ice with varying grain size in the range (1–1000 μm):

$$I/F_{\text{water\_ice}} = r_{\text{s\_regolith}} \langle \mu_0 \rangle r_{\text{s\_water\_ice}} \frac{1 - \cos(\alpha)^2}{2}, \quad (5)$$

where $(1 - \cos(\alpha)^2)/2$ is the result of the integration of the Lambert reflectance of the floor above the solid angle subtended by the illuminated rim. The resulting I/F is shown in Fig 10 for pure AMT and water ice deposit. With respect to direct illumination in this case the water ice deposit shows a remarkable red slope in the visible and near-infrared spectral range due to the modulation of the light scattered by the AMT illuminated rim. The water ice diagnostic

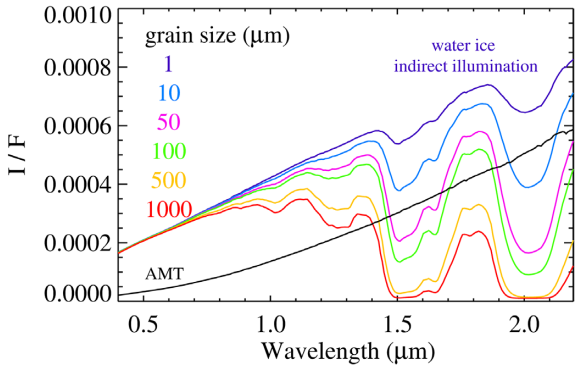

Figure 10. Simulated I/F spectra of a pure water ice deposit located on the PSR on the floor of Kandinsky crater indirectly illuminated by the portion of the crater rim bathed by the Sun. The six colour curves correspond to different water ice grain diameters from 1 to 1000 μm. The black curve is the I/F of the floor in case of AMT composition.

bands at 1.5–1.65 and at 2.0 μm are evident for all the simulated grain sizes and show a contrast with respect to the local continuum which increases with the grain size. The 1.05 and 1.25 μm bands become evident only for the larger grain sizes.

Noteworthy, MLA data taken over polar bright deposits show on average a reflectance at 1.064 μm approximately two times higher than over average terrains Deutsch et al. (2017). A similar behaviour is compatible with synthetic I/F spectra shown in Fig. 10 for the larger grain sizes (500–1000 μm). In case of areal mixing with small quantities (few per cent) of AMT even small water ice grains (1–100 s μm) would become compatible with a similar enhancement by a factor 2 on the I/F(1.064 μm).

6 VIHI SNR ORBITAL SIMULATIONS

With the aim to verify VIHI sensitivity above Mercury polar icy regions, we apply the instrumental radiometric model to the syntethic I/F spectra discussed in the previous Section 4 for the three possible illumination cases: (1) direct sunlight, (2) penumbra, and (3) shadowed areas detailed in the following.

6.1 Direct sunlight case

The direct sunlight case is the one offering the better signal-to-noise ratio (SNR) conditions. This case is representative for those conditions in which sunlight reaches the proximity of ice deposits in the PSR for certain TA conditions occurring during the solar day. Due to high solar thermal flux at Mercury (solar costant is 9082.7 W/m^2 at equator, about 6.7 times higher than on the Earth), among the three cases considered this one is the less probable to occur on ice deposits because recurrent direct illumination on each orbit will rapidly cause the sublimation of the deposit itself. This can be considered therefore as a best case. The computation of the SNR is performed starting from I/F syntethic spectra discussed in Section 4 for a given point at lat = ±80° for the changing observation conditions occurring along BepiColombo orbit. We report expected SNR sampled at TA = 0° (perihelion/apoherm), 45°, 60°, 120°, 135°, 180° (apohelion/periherm). The illumination conditions occurring for 180° ≤ TA ≤ 360° are symmetrical due to the Mercury orbital characteristics (Fig. 1). The majority of the VIHI observations are foreseen to be performed within a range of TA = ±45° from perihelion and aphelion. Cases at TA = 60° and 120° are simulated with the aim to evaluate the possibility to extend polar observation campaigns on a longer period of time and to optimize their timing with respect to solar azimuthal angle. Going towards TA = 90° and 270° the illumination worsens progressively because here BepiColombo is orbiting terminator's plane where the solar phase approaches 90°.

The spectral radiance S(λ) (in $Wm^{-2}\mu m^{-1}sr^{-1}$) from Mercury surface is computed as

$$S(\lambda, ZA) = I/F(\lambda, ZA)\frac{SI(\lambda)}{\pi \cdot D_{Sun}^2}, \quad (6)$$

where the solar ZA follows equation (3), $I/F(\lambda, ZA)$ is the radiance factor derived from equation (4) at a specific ZA, $SI(\lambda)$ is the solar spectral irradiance measured at 1 au (Thekekara 1973), and D_{Sun} the heliocentric distance (in au) which depends from orbital parameters and TA:

$$D_{Sun} = \frac{A(1-e^2)}{1+e\cdot\cos(TA)}, \quad (7)$$

where A = 0.387098 au is the Mercury orbit semimajor axis and e = 0.2056 is the eccentricity. For a given input, spectral radiance $S(\lambda)$ the VIHI expected signal, in Digital Numbers (DN), is given by

$$DN(\lambda) = S(\lambda)\cdot R(\lambda)\cdot t_{exp}, \quad (8)$$

where R(λ) is the VIHI responsivity from Filacchione et al. (2017) and t_{exp} is the integration time. As a result of the MPO spacecraft elliptical orbit around Mercury, the integration time needs to be tuned with respect to the dwell time (t_{dwell}), defined as the time necessary to move the projection of one pixel on the surface by one instantaneous field of view (IFOV = 250 μrad). Apart from IFOV value, it depends from spacecraft altitude (D) and sub-spacecraft point velocity (v_{sub}):

$$t_{dwell} = \frac{IFOV\cdot D}{v_{sub}}. \quad (9)$$

In order to avoid smearing, we assume a maximum integration time equal to 0.33 times the dwell time. The optimized integration times are selected to be compliant with the maximum integration time while avoiding saturation. For observations taken above a point at latitude ±80°, we are using integration time of 20 and 25 ms for the orbital arc around perihelion and aphelion, respectively. The simulations are performed assuming the nominal operative temperature of the detector (T = 220 K). With these parameters, the SNR ratio is computed as

$$SNR(\lambda) = \frac{DN\cdot\eta}{\sqrt{DN\cdot\eta + DN_{bkg}\cdot\eta}}, \quad (10)$$

where $\eta = 146\,(e^-/DN)$ is the A/D converter factor necessary to convert the number of photoelectrons accumulated on the detector in DN at the exit of the readout electronics. The η value is determined by dividing the detector's full-well capacity ($2\,Me^-$) by the dynamical range of the A/D converter (≈ 14.000 DN). The background and dark current photoelectrons DN_{bkg} were measured during the pre-launch radiometric calibration campaign (Filacchione et al. 2017, 2018). Due to the high linearity of the detector's response, the dark and background increase with t_{exp} according to

$$DN_{bkg}[DN] = 2160.58\,[DN] + 40.29\left[\frac{DN}{ms}\right]\cdot t_{exp}[ms] \quad (11)$$

at nominal operative temperature of the detector (220 K). This case is applied to both aphelion and perihelion observations cases.

The SNR spectra computed for icy mixtures and non icy (AMT) cases in direct illumination geometry across the full spectral range

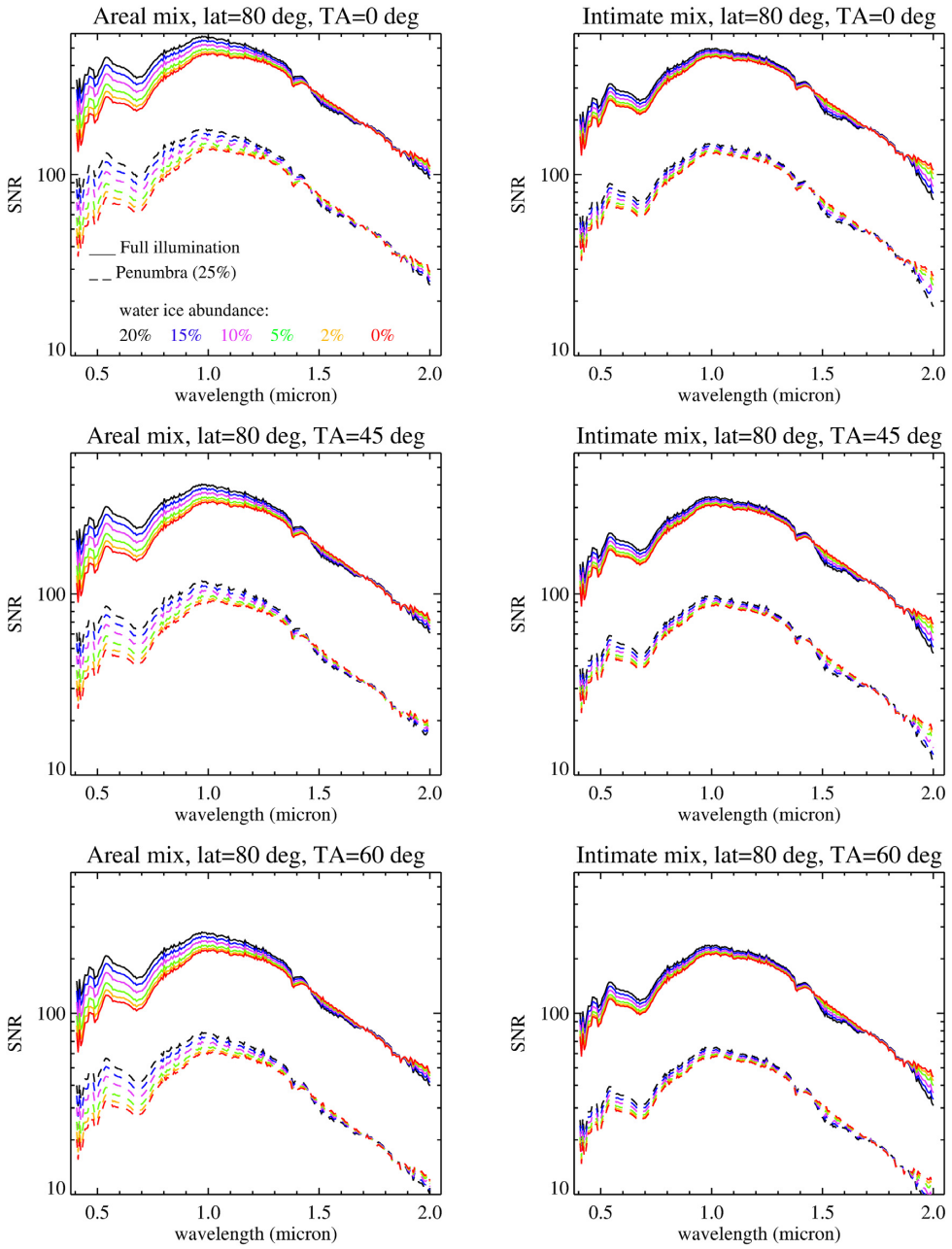

Figure 11. VIHI theoretical SNR in the direct illumination (the solid lines) and in the penumbra (efficiency of 25 per cent of the direct illumination, the dashed lines) for AMT–water ice mixtures from 100:0 per cent to 80:20 per cent abundances, 100 μm grain diameter, computed at latitude ±80° for perihelion orbital arc (from top to bottom TA = 0°, 45°, 60°). Areal and intimate mixing cases are shown on the left and right columns, respectively. Simulations are performed with i = 80° and e = 0°.

of VIHI are shown as the solid lines in Figs 11 and 12 for the aphelion (TA = 0°, 45°, 60°) and perihelion arc cases (120°, 135°, 180°), respectively. On each figure, the results for the areal (left column) and intimate mixing case (right column) are given.

The high responsivity of the VIHI spectrometer (up to 2000 DN m^2 sr μm W^{-1} s^{-1} at 1.2 μm) and the high radiance levels from Mercury's surface (up to about 500 W m^{-2} $μm^{-1}$ sr^{-1} at 1 μm for TA = 0°, lat = 0°) allow to achieve good SNR values for the simulated reflectances across the full 0–4–2.0 μm range. The SNR profiles are modulated by the instrumental responsivity curve that peaks at about 1.0 μm where the overall instrument efficiency is maximum. A secondary peak is at about 0.55 μm, while the overall efficiency decreases as a function of wavelength from 1.0 to 2.0 μm. The best SNR is obtained at perihelion (TA = 0°), while the values reached at aphelion (TA = 180°) are similar to the ones measured at TA = 60°. Since the instrument spectral range is limited at 2.05 μm and allows to retrieve only the left side of the 2 μm water ice band depth we limit our discussion to the 1.5–1.65 μm band, which is fully resolved. During the perihelion arc, the SNR on this spectral range is always well above 100, corresponding to an error on the I/F of $\leqslant$ 1 per cent (optimal case). This is observed for all simulated AMT–water ice mixtures from 100:0 to 80:20 abundances in both areal and intimate mixing modalities. The SNR is worse during the

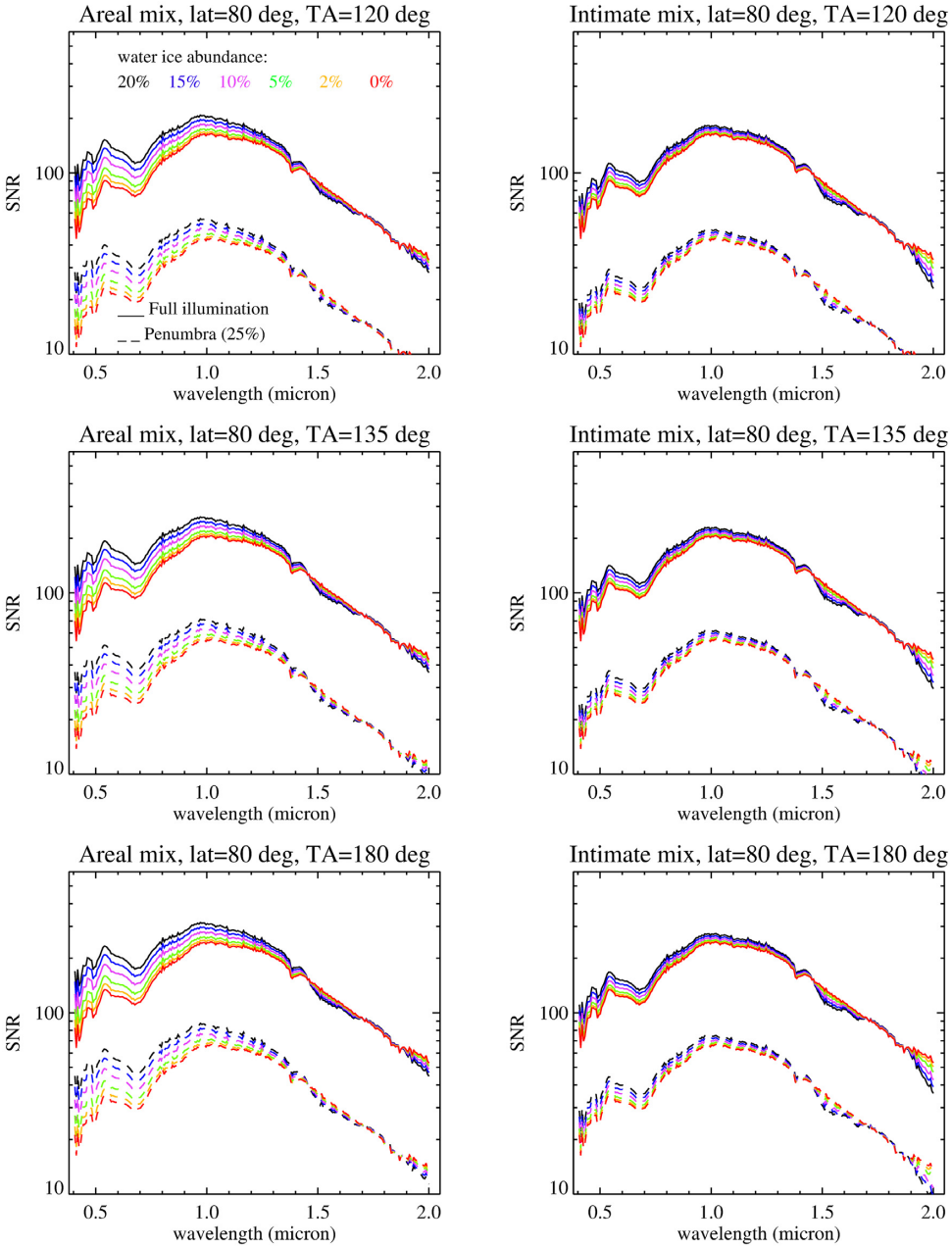

Figure 12. VIHI theoretical SNR in the direct illumination (the solid lines) and in the penumbra (efficiency of 25 per cent of the direct illumination, the dashed lines) for AMT–water ice mixtures from 100:0 per cent to 80:20 per cent abundances, 100 μm grain diameter, computed at latitude ±80° for aphelion orbital arc (from top to bottom TA = 120°, 135°, 180°). Areal and intimate mixing cases are shown on the left and right columns, respectively. Simulations are performed with i = 80° and e = 0°.

aphelion arc, where it is ≥100 only at TA = 135°–180° for both areal and intimate mixing case.

6.2 Penumbra case

The same methodology to compute the SNR in direct illumination case is applied to the spectral simulations on areas in penumbra. As shown in Section 2 in this case the illumination is distributed with a gradient within the penumbra length with efficiency changing from 100 per cent of the full illumination side to 0 per cent for the full shadow side. As a test case, we simulate the SNR for an efficiency of 25 per cent of the full illumination corresponding to a distance of about 1/4 of the penumbra length from the shadow boundary. The SNR is computed for this case by reducing the solar flux of 1/4 in equation (6) and maintaining all the simulation parameters used for the direct illumination case in Section 6.1. The results are shown as the dashed line in Figs 11–12 for the aphelion (TA = 0°, 45°, 60°) and perihelion arc cases (120°, 135°, 180°), respectively. Across the penumbra area a strong illumination gradient is established, resulting in very variable SNR conditions: between the direct illumination case (the solid curve) and the 25 per cent attenuation case (the dashed curves) a decrease of the SNR by a factor ≈4.5 is observed on all cases.

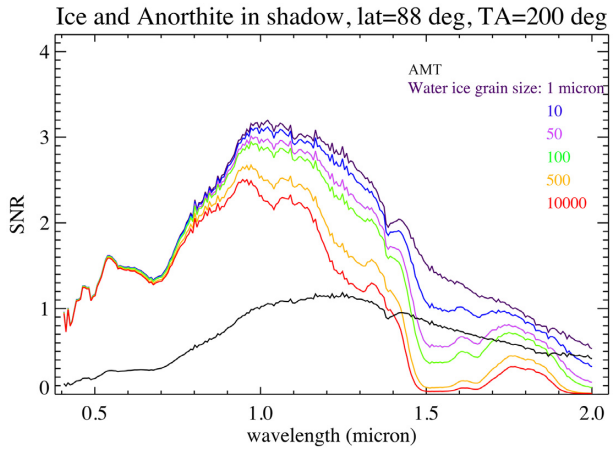

Figure 13. VIHI theoretical SNR for the floor of Kandinsky crater assuming a composition made of AMT or pure water ice with grain diameters between 1 and 1000 μm. The simulation is applicable to the shadowed area on the centre of the crater illuminated by the scattered light coming from the nearby sun-bathed rim (see Fig. 9). Simulations are performed at TA = 200° and with an exposure time of 50 ms.

6.3 Indirect sunlight or shadowed case

As said, the shadowed case is representative of ice deposits in PSR never directly illuminated by the Sun nor by penumbras. The SNR simulation in this case is computed adopting the I/F given in equation (5) in the radiance equation (6). In particular, we apply this method to the ice deposit on Kandinsky crater, previously discussed in Section 5, for the illumination conditions occurring at TA = 200° rendered in Fig. 9. Given the orbital position of Mercury, this can be considered as a worst case for the radiometric simulations because the solar flux is the lowest among all cases considered in this work and the intrinsic I/F of the putative ice deposit is very low as well ($\leq 8 \times 10^{-4}$ at 1.8 μm, see Fig. 10). As a consequence of these conditions, the SNR associated with the water ice spectra shown in Fig. 13 is only $\lesssim$3. These simulations are performed with an extended exposure time t_{exp} = 50 ms in order to improve as much as possible the signal while remaining compatible with the dwell time constraint (equation 9).

Despite being very low, the SNR ratio of the central deposit shows some distinctive properties between the pure AMT and pure water ice cases which pair with the I/F spectral properties discussed in Fig. 10. These properties can be exploited to discriminate between the two cases and to infer the water ice grain size distribution. In the 1.0–1.1 μm range the higher I/F of water ice with respect to the AMT allows to reach higher SNR by a factor 3 on micron-sized particles and by a factor 2 on millimeter-sized ones. Across the diagnostic water ice band at 1.5–1.65 μm the SNR conditions are mixed between the two compositions: small water ice grains (1–10 μm) offer an SNR a bit larger than AMT SNR ($\approx$1), while on large grains (0.5-1 mm) the SNR is null.

7 CONCLUSIONS

The study of the ice deposits on PSRs at Mercury poles is one of the primary BepiColombo scientific investigations (Rothery et al. 2020) to which SIMBIO-SYS/VIHI will give a major contribution. VIHI data will offer for the first time the opportunity to detect and map ices composition, abundance, grain size, and mixing modalities by means of visible and infrared observations. We have shown in this work how water ice surface deposits can be detected on the vicinity of the PSRs under temporary direct illumination and penumbra and within PSRs under indirect illumination conditions. On both cases, the detection of the diagnostic spectral features at 1.05, 1.25, 1.5–1.65, and 2.0 μm will allow to asses the presence of water ice. By applying radiative models for specific illumination/viewing geometries it is possible to simulate the presence of superficial water ice in terms of abundance, grain size, and mixing modalities with mineral phases. Moreover, having characterized the VIHI radiometric performances and used a wide range of possible water ice enrichments by means of simulations, we assess that the instrument has sufficient sensitivity (SNR $\geq$ 100) to detect water ice up to few per cent abundances mixed with AMT regolith on direct sunlight areas and in many penumbra cases during both perihelion and aphelion mission phases. The identification of ices in shadowed areas is more challenging and needs to address several issues both in terms of observations planning and execution, and data modelling and processing. The complex morphology and changing illumination conditions on polar regions need to be taken into account during the planning of the observations with the scope to maximize signal and surface coverage. Several strategies can be adopted in this regard, from preferring observations near perihelion when the solar flux is higher, to stack and average data from successive orbits or to relax the smearing requirement to improve SNR. This will be facilitated by the high level of redundancy on polar regions because of the BepiColombo orbital parameters. Another possibility is to take advantage of the great excursion in TA to identify specific illumination geometries able to maximize the scattered light within the PSRs. This will need accurate 3D digital models of the polar regions necessary to simulate the incident and scattered lightpaths. Past experiences acquired on similar imaging spectrometers such as VIRTIS onboard Rosetta (Coradini et al. 2007) and VIR on Dawn (De Sanctis et al. 2011) have shown that spectral identification of ices is still achievable in very poor SNR conditions typical of very dark terrains and scarce illumination conditions: apart the case of the Juling crater on Ceres (Raponi et al. 2018) mentioned before in Section 5, similar conditions were exploited on comet 67P/Churyumov–Gerasimenko to identify superficial water (De Sanctis et al. 2015; Filacchione et al. 2016b) and carbon dioxide (Filacchione et al. 2016a) ices at very low radiance levels. For the future, we are aiming to extend spectral simulations to other icy species stable at hermean temperatures within PSRs, as suggested by Paige et al. (2013). Furthermore, we plan to investigate the nature of the dark deposits observed at lower latitudes (Lawrence et al. 2013). These deposits are probably rich in carbonaceous species and organic matter, blanketing the ices buried below them. Our simulations show the capability of the VIHI spectrometer to detect water ice presence in the polar regions of Mercury up to few per cent abundances. With similar performances, we expect to be able to improve our knowledge of composition, distribution, and mass of ices hosted at Mercury's poles. In this respect, the availability of high-resolution colour images by HRC and DTMs by STC acquired at the same time of VIHI hyperspectral data will offer an unprecedented opportunity for the SIMBIO-SYS investigation to progress in the characterization of the hermean polar ices. Finally, this investigation will benefit from both coordinated observations with other instruments (BELA, MERTIS, MGNS) aboard BepiColombo mission and from thermo-physical models. The first will provide different ice detection techniques allowing to confirm their presence by means of independent measurements. The latter will allow to study local temperature variations with the aim to constrain ice deposition processes, seasonal variability and

total mass. These activities are currently ongoing within the ESA BepiColombo mission and instrument teams.

ACKNOWLEDGEMENTS

The authors acknowledge the financial support from Italian Space Agency (ASI) to the Istituto Nazionale di Astrofisica (contracts I/022/1070 and 2017-47-H.0) and technical support of Leonardo Company S.p.A. (Campi Bisenzio-Florence, Italy), prime industrial contractor of the SIMBIO-SYS instrument. This research has used NASA's Astrophysics Data System.

DATA AVAILABILITY STATEMENT

MESSENGER DEM data are produced by the MLA Science Team at the NASA / Goddard Space Flight Center, Greenbelt, Maryland and are publicly available through NASA PDS Geosciences node at https://pds-geosciences.wustl.edu/missions/messenger/mla.htm. Illumination renderings on DEM simulated by means of ISIS codes are available as Supplementary Material. Spectral modelling simulations and SNR simulations will be shared on reasonable request to the corresponding author.

REFERENCES

Benkhoff J. e., 2020, Space Sci. Rev., submitted
Capaccioni F. et al., 2010, IEEE Trans. Geosci. Remote Sens., 48, 3932
Cavanaugh J. F. et al., 2007, Space Sci. Rev., 131, 451
Chabot N. L. et al., 2014, Geology, 42, 1051
Chabot N. L. et al., 2016, Geophys. Res. Lett., 43, 9461
Chabot N. L., Shread E. E., Harmon J. K., 2018, J. Geophys. Res., 123, 666
Ciarniello M. et al., 2011, Icarus, 214, 541
Clark R. N. et al., 2012, Icarus, 218, 831
Coradini A. et al., 2007, Space Sci, Rev., 128, 529
Cremonese G. et al., 2020, Space Sci. Rev., 216, 75
Da Deppo V., Naletto G., Cremonese G., Calamai L., 2010, Appl. Opt., 49, 2910
De Sanctis M. C. et al., 2011, Space Sci. Rev., 163, 329
De Sanctis M. C. et al., 2015, Nature, 525, 500
Deutsch A. N., Chabot N. L., Mazarico E., Ernst C. M., Head J. W., Neumann G. A., Solomon S. C., 2016, Icarus, 280, 158
Deutsch A. N., Neumann G. A., Head J. W., 2017, Geophys. Res. Lett., 44, 9233
Domingue D. L., D'Amore M., Ferrari S., Helbert J., Izenberg N. R., 2019a, Icarus, 319, 140
Domingue D. L., D'Amore M., Ferrari S., Helbert J., Izenberg N. R., 2019b, Icarus, 319, 247
Ernst C. M., Chabot N. L., Barnouin O. S., 2018, J. Geophys. Res., 123, 2628
Filacchione G. et al., 2016a, Science, 354, 1563
Filacchione G. et al., 2016b, Nature, 529, 368
Filacchione G. et al., 2017, Rev. Sci. Instrum., 88, 094502
Filacchione G. et al., 2018, 5th IEEE International Workshop on Metrology for AeroSpace (MetroAeroSpace, IEEE Xplore, Rome, p. 252
Hapke B., 1993, Theory of reflectance and emittance spectroscopy,, Cambridge University Press, Cambridge, UK
Hapke B., 2005, Theory of Reflectance and Emittance Spectroscopy, Cambridge University Press, Cambridge, UK
Hapke B., 2012, Icarus, 221, 1079
Harmon J. K., Slade M. A., Vélez R. A., Crespo A., Dryer M. J., Johnson J. M., 1994, Nature, 369, 213
Harmon J. K., Slade M. A., Rice M. S., 2011, Icarus, 211, 37
Head J. W. et al., 2011, Science, 333, 1853
Jones B. M., Sarantos M., Orlando T. M., 2020, ApJ, 891, L43
Lawrence D. J. et al., 2013, Science, 339, 292
Mastrapa R. M., Bernstein M. P., Sandford S. A., Roush T. L., Cruikshank D. P., Dalle Ore C. M., 2008, Icarus, 197, 307
Neumann G. A. et al., 2013, Science, 339, 296
Paige D. A., Wood S. E., Vasavada A. R., 1992, Science, 258, 643
Paige D. A. et al., 2013, Science, 339, 300
Raponi A. et al., 2018, Sci. Adv., 4, eaao3757
Rothery D. A. et al., 2020, Space Sci. Rev., 216, 66
Rubanenko L., Mazarico E., Neumann G. A., Paige D. A., 2018, J. Geophys. Res., 123, 2178
Siegler M. A., Bills B. G., Paige D. A., 2013, J. Geophys. Res., 118, 930
Slade M. A., Butler B. J., Muhleman D. O., 1992, Science, 258, 635
Solomon S. C., McNutt R. L., Gold R. E., Domingue D. L., 2007, Space Sci. Rev., 131, 3
Thekekara M. P., 1973, Sol. Energy, 14, 109
Vander Kaaden K. E., McCubbin F. M., 2015, J. Geophys. Res., 120, 195
Warell J., Blewett D. T., 2004, Icarus, 168, 257
Warren S. G., 1984, Appl. Opt., 23, 1206
Watson K., Murray B., Brown H., 1961a, J. Geophys. Res., 66, 1598
Watson K., Murray B. C., Brown H., 1961b, J. Geophys. Res., 66, 3033
Zusi M., Paolinetti R., Corte V. D., Marra G., Baroni M., Palumbo P., Cremonese G., 2019, Appl. Opt., 58, 4059

SUPPORTING INFORMATION

Supplementary data are available at *MNRAS* online.

Figure 4. Illumination rendering on the north polar regions for TA = 200°.

Please note: Oxford University Press is not responsible for the content or functionality of any supporting materials supplied by the authors. Any queries (other than missing material) should be directed to the corresponding author for the article.

This paper has been typeset from a TEX/LATEX file prepared by the author.